Bioactive Materials 32 (2024) 530–542

Contents lists available at ScienceDirect

Bioactive Materials

journal homepage: www.keaipublishing.com/en/journals/bioactive-materials

Bioresponsive and immunotherapeutic nanomaterials to remodel tumor microenvironment for enhanced immune checkpoint blockade

Tianxu Fang [a,b], Xiaona Cao [a,b], Li Wang [a,b], Mo Chen [a,b], Yueyang Deng [a,b], Guojun Chen [a,b,*]

[a] Department of Biomedical Engineering, McGill University, Montreal, QC, H3G 0B1, Canada
[b] Rosalind & Morris Goodman Cancer Institute, McGill University, Montreal, QC, H3G 0B1, Canada

ARTICLE INFO

Keywords:
Tumor microenvironment
Immune modulation
Calcium carbonate nanoparticles
Cancer immunotherapy
Immune checkpoint inhibitor
Drug delivery

ABSTRACT

Immune checkpoint blockade (ICB) therapy is a revolutionary approach to treat cancers, but still have limited clinical applications. Accumulating evidence pinpoints the immunosuppressive characteristics of the tumor microenvironment (TME) as one major obstacle. The TME, characterized by acidity, hypoxia and elevated ROS levels, exerts its detrimental effects on infiltrating anti-tumor immune cells. Here, we developed a TME-responsive and immunotherapeutic catalase-loaded calcium carbonate nanoparticles (termed as CAT@$CaCO_3$ NPs) as the simple yet versatile multi-modulator for TME remodeling. $CaCO_3$ NPs can consume protons in the acidic TME to normalize the TME pH. CAT catalyzed the decomposition of ROS and thus generated O_2. The released Ca^{2+} led to Ca^{2+} overload in the tumor cells which then triggered the release of damage-associated molecular patterns (DAMP) signals to initiate anti-tumor immune responses, including tumor antigen presentation by dendritic cells. Meanwhile, CAT@$CaCO_3$ NPs-induced immunosupportive TME also promoted the polarization of the M2 tumor-associated macrophages to the M1 phenotype, further enhancing tumor antigen presentation. Consequently, T cell-mediated anti-tumor responses were activated, the efficacy of which was further boosted by aPD-1 immune checkpoint blockade. Our study demonstrated that local treatment of CAT@$CaCO_3$ NPs and aPD-1 combination can effectively evoke local and systemic anti-tumor immune responses, inhibiting the growth of treated tumors and distant diseases.

1. Introduction

Immunotherapy has undeniably revolutionized cancer treatment by harnessing the inherent capabilities of the immune system to combat malignancies [1,2]. Particularly, immune checkpoint blockade (ICB) therapy, has achieved promising clinical progress in many malignancies, including triple-negative breast cancer, melanoma, non-small cell lung, renal cell carcinoma, urothelial carcinoma, bladder, and head and neck cancers [3]. However, despite these achievements of ICB in the clinic, many challenges remain to be overcome, particularly the low objective response rate of ICB therapy. The tumor microenvironment (TME) has been ascertained as one of the major obstacles in ICB therapy due to its detrimental impacts on tumor-infiltrating immune cells and the following anti-immune activities [4].

TME is characteristically immunosuppressive, which significantly suppresses the efficacy of effector immune cells against cancer cells [5,6]. The TME comprises an intricate web of tumor cells and the surrounding extracellular matrix (ECM), tumor vasculature, stromal cells, immune cells, and various chemokines and cytokines [7–10]. The immunosuppressive TME includes many physicochemical abnormalities, such as tumor acidity, hypoxia, and high levels of reactive oxygen species (ROS), which is mainly attributed to abnormal metabolism in tumor tissues [11–15]. These physicochemical abnormalities play an important role in inducing an immunosuppressive microenvironment in tumors by activating the immunosuppressive cells and defunctionalizing the immune-active cells, especially tumor-infiltrating lymphocytes (TIL) [16–20]. Specifically, the acidic, oxidative and hypoxic environment in tumor inhibits the differentiation, maturation and cell-presenting ability of dendritic cells (DC), as well as the infiltration, survival, and cytotoxic activity of T cells, and promotes the skewing of tumor-associated macrophages (TAM) to the immunosuppressive M2 phenotype, and the accumulation of immunosuppressive regulatory T cells (Treg) and myeloid-derived suppressor cells (MDSC) [21–23]. Hence, strategies for normalizing pH, reducing ROS levels, and relieving hypoxia within TME

Peer review under responsibility of KeAi Communications Co., Ltd.
* Corresponding author. Department of Biomedical Engineering, McGill University, Montreal, QC, H3G 0B1, Canada.
E-mail address: guojun.chen@mcgill.ca (G. Chen).

https://doi.org/10.1016/j.bioactmat.2023.10.023
Received 1 September 2023; Received in revised form 20 October 2023; Accepted 23 October 2023

to foster an immunosupportive TME are needed. While there are approaches to tackle one individual abnormality, a simple strategy that can simultaneously target all three environmental abnormalities within TME is lacking.

In this study, we reported a TME-responsive nanomaterials, namely catalase-loaded calcium carbonate nanoparticles (termed as CAT@$CaCO_3$ NPs), as a simple yet versatile multi-modulator to reverse immunosuppressive TME and enhance the activities of anti-tumor immune cells, thus amplifying efficacy of ICB (Fig. 1). To overcome hypoxia in TME, producing oxygen *in situ* in tumor tissues could be more effective than delivering oxygen gas into the tumors [24–26]. ROS, abundant within the TME can be an excellent source of oxygen when catalytically degraded by natural antioxidants, such as catalase (CAT) [27–33]. Hence, CAT not only relieves hypoxia but also mitigates the high ROS levels in the TME. In the meantime, to normalize TME acidity, pH-responsive calcium carbonate nanoparticles ($CaCO_3$ NPs), a widely used drug delivery vehicle with excellent biocompatibility and biodegradability [34–36], were employed, which can consume the excessive protons. Additionally, by encapsulating CAT in $CaCO_3$ NPs, the enzymatic activity of CAT can be prolonged by preventing CAT from rapid degradation *in vivo*. Therefore, CAT@$CaCO_3$ NPs serve as a simple multi-modulator capable of reprogramming the immunosuppressive TME into an immunosupportive environment. Moreover, over-accumulation of Ca^{2+} released from $CaCO_3$ NPs can effectively induce the release of damage-associated molecular patterns (DAMP) signals from tumor cells through mitochondrial damaging [37–40]. DAMPs, hallmarks of immunogenic cell death (ICD), then promote presentation of tumor associated antigens (TAAs) by the antigen-presenting cells, such as DC, which further facilitate T cell priming and activation [41–43]. CAT@$CaCO_3$ NPs treatment can also promote the polarization of TAMs from M2 phenotype to M1 phenotype, further enhancing the tumor-antigen presenting abilities. Taken together, CAT@$CaCO_3$ NPs treatment can remodel the TME, fostering an immunosupportive milieu conducive to activating T-cell-mediated anti-tumor immunity, the efficacy of which can be further potentiated by anti-programmed death 1 antibody (aPD-1)-mediated ICB therapy. Our results indicated that the local treatment of combined CAT@$CaCO_3$ NPs and aPD-1 awakened both local and anti-tumor immunity, exhibiting robust immunotherapeutic efficiencies in primary and distant diseases.

2. Materials and methods

2.1. Materials, cells and animals

4-benzyl L-aspartate acid (BLA) was purchased from Thermo Scientific. Methoxypolyethylene glycol amine and sodium carbonate (Na_2CO_3) were bought from Fisher Scientific. Calcium chloride ($CaCl_2$) was obtained from Alfa Aesar. Catalase was purchased from Sigma-Aldrich. aPD-1 was obtained from BioLegend (Cat no. 135235). The murine 4T1 cells were obtained from Peter Siegel's Lab at McGill University. 4T1 cells were cultured in Dulbecco's modified Eagle medium (DMEM) (Gibco) with 10 % fetal bovine serum (FBS) (Gibco), 1 % penicillin/streptomycin (Gibco), 2 % sodium bicarbonate (Gibco), 1 % 1 M N-2-hydroxyethylpiperazine-N-2-ethane sulfonic acid (HEPES) (Gibco), 1 % sodium pyruvate (Gibco). BALB/c mice (6–7 weeks) were purchased from Charles River Laboratories. All animal-related experiments were carried out following the animal protocol approved by McGill University.

2.2. Synthesis and characterization of poly (4-benzyl L-aspartate acid)-polyethylene glycol block copolymer

15 mmol of triphosgene in 10 mL anhydrous tetrahydrofuran (THF) was added over a 30 min period to 30 mmol BLA in 50 mL anhydrous THF. The mixture was stirred at 55 °C for 3 h until a clear solution was observed. The solution was poured into 100 mL hexane and the suspension was stored overnight at −20 °C to for crystallization. White precipitates were collected and dried under vacuum at room temperature to obtain BLA-N-carboxy anhydride (NCA) (Fig. S1).

600 mg of prepared BLA-NCA was dissolved with 200 mg of methoxypolyethylene glycol amine in 10 mL of dimethylformamide (DMF). The reaction was continued at 55 °C for 72 h while stirring. The

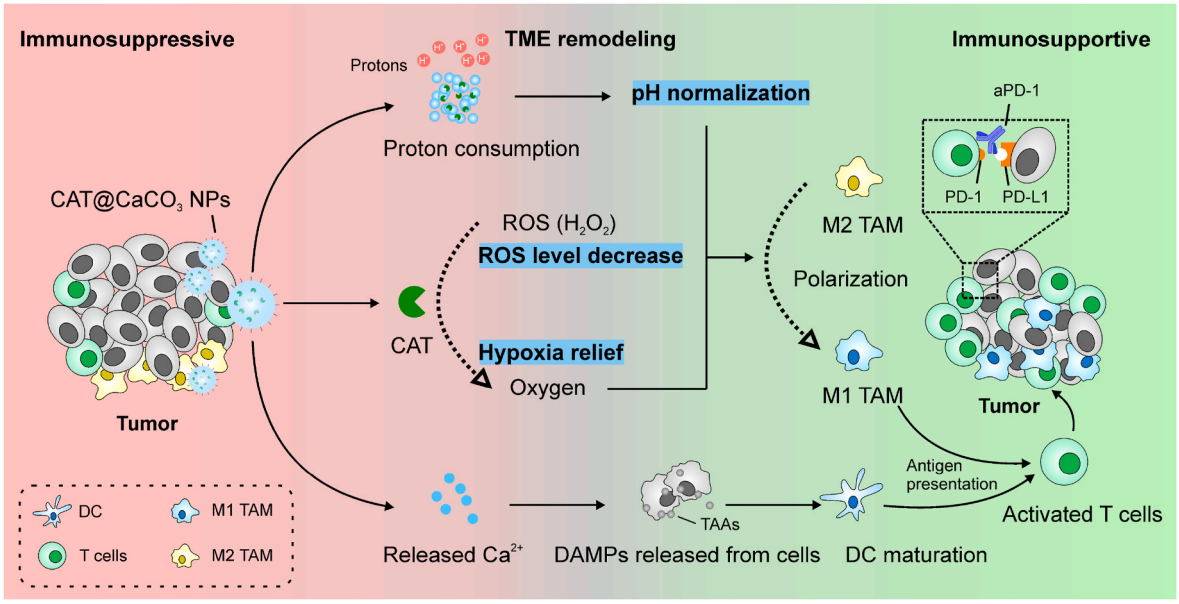

Fig. 1. CAT@$CaCO_3$ NPs remodels immunosuppressive TME to immunosupportive TME for enhanced ICB therapy. In the acidic TME, CAT@$CaCO_3$ NPs consumed protons to normalize the pH. CAT catalyzed the decomposition of hydrogen peroxide and produce oxygen, so as to lower the high ROS level and relieve the hypoxia in the TME. The remodeled TME promoted the polarization of M2 tumor-associated macrophages to M1 macrophages. The accumulated Ca^{2+} induced the release of DAMPs from tumor cells and initiated tumor antigen presentation, DC maturation and T-cell-mediated immune activation. aPD-1 further potentiated the anti-tumor effect of T cells. CAT: catalase; ROS: reactive oxygen species; TAAs: tumor-associated antigens; DAMPs: damage-associated molecular patterns; DC: dendritic cells; TAM: tumor-associated macrophages; PD-1: programmed cell death 1; PD-L1: programmed cell death 1 ligand 1; aPD-1: programmed cell death 1 antibody; TME: tumor microenvironment.

product was precipitated in 80 mL cold diethyl ether for 24 h before centrifuging at 5000 rpm for 5 min. The supernatant was discarded, and the precipitation was dried for 10 min before redissolving in 3 mL DMF. The product was hydrolyzed for 2 h with 10 mL of 1 M NaOH. DMF was removed by dialysis for 48 h using the dialysis bag (MWCO 3.5 kD). The dialyzed solution was lyophilized to obtain poly (4-benzyl L-aspartate acid)-polyethylene glycol (PBLA-PEG) block copolymer (Fig. S1).

2.3. Preparation and characterizations of catalase-loaded calcium carbonate nanoparticles

1 mL of tris(hydroxymethyl)aminomethane (Tris)-HCl buffer (1 mM, pH 7.6) containing 100 mM $CaCl_2$ was mixed with 1 mL HEPES saline buffer (50 mM, pH 7.1, NaCl 140 mM) containing 1 mg catalase and 10 mg PBLA-PEG block copolymers. 1 mL of HEPES saline buffer containing 10 mM Na_2CO_3 was added dropwise while the solution was stirring. The reaction was left to run overnight at 4 °C, and the solution was collected for lyophilization to obtain the catalase-loaded calcium carbonate nanoparticles (termed as CAT@$CaCO_3$ NPs) after dialysis with the dialysis bag (molecular weight cutoff (MWCO) 3.5 kD). The blank calcium carbonate nanoparticles without loading catalase (termed as $CaCO_3$ NPs) were prepared with the similar process. The average particle size and zeta-potential of prepared CAT@$CaCO_3$ NPs were measured by a size analyzer. The morphology of CAT@$CaCO_3$ NPs was observed using transmission electron microscopy (TEM). To detect the loading efficiency of CAT, the supernatant with free CAT was collected after centrifuging CAT@$CaCO_3$ NPs at 12000 rpm. The CAT loading efficiency was calculated according to the equation below: Loading efficiency (%) = $(W_{total} - W_{free})/W_{NPs} \times 100$ %, where W_{total} and W_{free} were the amount of catalase used for CAT@$CaCO_3$ NPs preparation and unloaded in nanoparticles, respectively. W_{NPs} represented the total weight of nanoparticles sediment. The concentration of CAT was measured by the Bradford protein assay.

2.4. pH normalization, H_2O_2 scavenging, and oxygen generation in solutions

Catalase, $CaCO_3$ NPs (catalase 100 μg/mL, the concentration of $CaCO_3$ NPs was calculated based on the loading efficiency of catalase), or CAT@$CaCO_3$ NPs (catalase 10–200 μg/mL) was added in pH 6.5 phosphate buffered saline (PBS), and the pH of the solution was detected by a pH meter (pH 700, OAKTON).

Catalase, $CaCO_3$ NPs (catalase 100 μg/mL, the concentration of $CaCO_3$ NPs was calculated based on the loading efficiency of catalase), or CAT@$CaCO_3$ NPs (catalase 10–200 μg/mL) was added in 300 mM H_2O_2 solution, and the H_2O_2 concentration was measured using the hydrogen peroxide assay kit (Abcam).

Catalase, $CaCO_3$ NPs (catalase 100 μg/mL, the concentration of $CaCO_3$ NPs was calculated based on the loading efficiency of catalase), or CAT@$CaCO_3$ NPs (catalase 10–200 μg/mL) was added in 300 mM H_2O_2 solution containing tris(4,7-diphenyl-1,10-phenanthroline) ruthenium (II) dichloride (Ru (dpp)). Ru (dpp) is an oxygen sensor which quenches its fluorescence (λ_{ex} = 488 nm, λ_{em} = 610 nm) when exposed to oxygen [44–46], based on which the oxygen generation efficiencies were calculated.

2.5. Intracellular O_2 levels

4T1 cells were seeded in 24-well plates for 24 h and incubated with catalase, $CaCO_3$ NPs, or CAT@$CaCO_3$ NPs (catalase 100 μg/mL, the concentration of $CaCO_3$ NPs was calculated based on the loading efficiency of catalase) for 24 h. The cells were dyed Ru (dpp) for 1 h and examined with flow cytometry.

2.6. In vitro HIF-1α expression

4T1 cells were seeded in 6-well plates with glass slides for 24 h and incubated with catalase, $CaCO_3$ NPs, or CAT@$CaCO_3$ NPs (catalase 100 μg/mL, the concentration of $CaCO_3$ NPs was calculated based on the loading efficiency of catalase) for 24 h. All cells were cultured in the pH 6.5 culture media containing 50 μM H_2O_2 in a hypoxic atmosphere (5 % CO_2, 94 % N_2, 1 % O_2) [47–49]. The treated 4T1 cells were stained with hypoxia-inducible factor 1-α (HIF-1α) primary antibody (NOVUS, Cat no. NB100-654) and the corresponding secondary antibody (Invitrogen, fluorescein-labeled, Cat no. F2765). The fluorescent images were captured using laser scanning confocal microscopy (LSCM) (Observer. Z1, Zeiss). The fluorescent intensities of HIF-1α were quantified using ImageJ software. The protein samples in the treated cells were collected and separated using sodium dodecyl sulfate-polyacrylamide gel electrophoresis (SDS-PAGE). HIF-1α and β-tubulin were stained with corresponding primary antibodies (HIF-1α: NOVUS, Cat no. NB100-654; β-tubulin: Invitrogen, Cat no. PA5-16863) and the secondary antibody (Invitrogen, horseradish peroxidase (HRP)-labeled, Cat no. 65–1620) and shown on the films.

2.7. In vitro release of catalase

CAT@$CaCO_3$ NPs or 20 % Pluronic F127 hydrogels containing CAT@$CaCO_3$ NPs (CAT@$CaCO_3$ NPs-gel) was incubated in 8 mL of pH 7.4 or 6.5 PBS, the releasing media, at 37 °C and 100 rpm shaking. 500 μL of releasing media was collected for detection and substituted with the same amount of new releasing media. The extracted samples were centrifuged at 12000 rpm, 4 °C to collect the supernatant. The released catalase in the supernatant was detected using the Bradford protein assay.

2.8. Catalytic ability

The catalytic ability of catalase was detected using standard Goth's method [49–51]. Catalase or CAT@$CaCO_3$ NPs (catalase 100 μg/mL, with or without pre-treatment with 0.5 mg/mL protease K for 30 min at 37 °C) was added into pH 7.4 or 6.5 PBS containing H_2O_2. 32.4 mM ammonium molybdate was added to terminate the catalytic reaction. The remained H_2O_2 reacted with ammonium molybdate to generate stable primrose yellow complex (characteristic absorption at 400 nm). The absorbance of the complex was compared with the free catalase without protease K pre-treatment in pH 7.4 solution as the control to calculate the catalytic ability.

2.9. Cellular uptake

4T1 cells were seeded in 24-well plates and cultured for 24 h. Then, the cells were incubated with fluorescein isothiocyanate (FITC)-labeled catalase (termed as FITC-CAT) or FITC-CAT-loaded calcium carbonate nanoparticles (termed as FITC-CAT@$CaCO_3$ NPs) for 4 h with the catalase concentration of 100 μg/mL. The cells were collected and analyzed using flow cytometry (LSRFortessa, BD).

2.10. Intracellular calcium ion level and mitochondrial damage

4T1 cells were seeded in 24-well plates for 24 h and incubated with catalase, $CaCO_3$ NPs, or CAT@$CaCO_3$ NPs (catalase 100 μg/mL, the concentration of $CaCO_3$ NPs was calculated based on the loading efficiency of catalase) for 24 h. Calcium chloride with the same amount of Ca ions as $CaCO_3$ NPs was also used for comparison. The cells were stained with Fluo-3 AM, the intracellular calcium indicator [52,53], or JC-1, the mitochondrial membrane potential assay kit [54,55], for 1 h and analyzed using flow cytometry.

2.11. Cytotoxicity and release of DAMP signals

4T1 cells were seeded in the 96-well plates (lower chamber) for 24 h and then incubated with 20 % Pluronic hydrogel (termed as blank gel), CAT@$CaCO_3$ NPs or CAT@$CaCO_3$ NPs-gel in transwells (upper chamber) for 24 h. The concentration of CAT ranged from 0 to 100 μg/mL, and the amount of Pluronic hydrogel was calculated by the ratio of 1 mg of CAT per 400 μL 20 % Pluronic hydrogel. The cell viabilities were detected using 3-(4,5-dimethylthiazol-2-yl)-2,5-diphenyl-2H-tetrazolium bromide (MTT) assay.

4T1 cells were seeded in 24-well plates for 24 h and then incubated with catalase, $CaCO_3$ NPs, or CAT@$CaCO_3$ NPs (catalase 100 μg/mL, the concentration of $CaCO_3$ NPs was calculated based on the loading efficiency of catalase) for 24 h, and collected for staining with calreticulin (CRT) primary antibody (Invitrogen, Cat no. PA3-900) and an Alexa Fluor 555-labeled secondary antibody (Invitrogen, Cat no. A21428). The expression of CRT was measured using flow cytometry. The adenosine triphosphate (ATP) concentrations in the lysed tumor cells and released in the culture media were measured by the ATP determination kit (Invitrogen). 4T1 cells growing on the glass slides were stained with high mobility group box 1 (HMGB1) primary antibody (Invitrogen, Cat no. PA5-27378) and a fluorescein-labeled secondary antibody (Invitrogen, Cat no. F2765). The fluorescent images were captured using LSCM(Observer. Z1, Zeiss). The fluorescent intensities of HMGB1 were quantified using ImageJ software.

2.12. In vitro DC maturation

4T1 cells were seeded in the transwells (upper chamber), and incubated with catalase, $CaCO_3$ NPs, or CAT@$CaCO_3$ NPs (catalase 100 μg/mL, the concentration of $CaCO_3$ NPs was calculated based on the loading efficiency of catalase) for 24 h. DCs were seeded in the 24-well plates (lower chamber) and cocultured with the treated cells in the transwells for another 24 h. All cells were cultured in the pH 6.5 culture media containing 100 μM H_2O_2 in a hypoxic atmosphere (5 % CO_2, 94 % N_2, 1 % O_2). DCs were then harvested for staining with the APC-labeled CD11c (BioLegend, Cat no. 117310), the Pacific Blue-labeled CD80 (BioLegend, Cat no. 104724) and the phycoerythrin (PE)-labeled CD86 antibodies (BioLegend, Cat no. 105008), and analyzed by flow cytometry.

2.13. In vitro macrophage polarization

Tumor cells were seeded in the transwells (upper chamber) and incubated with catalase, $CaCO_3$ NPs, or CAT@$CaCO_3$ NPs (catalase 100 μg/mL, the concentration of $CaCO_3$ NPs was calculated based on the loading efficiency of catalase) for 24 h. Macrophages were seeded in the 24-well plates (lower chamber) and cultured with the treated cells in the transwells for another 24 h. All cells were cultured in the pH 6.5 culture media containing 100 μM H_2O_2 in a hypoxic atmosphere (5 % CO_2, 94 % N_2, 1 % O_2). The macrophages were harvested for staining with the PE-labeled CD11b (BioLegend, Cat no. 101208) and the Pacific Blue-labeled CD80 (BioLegend, Cat no. 104724) for M1 macrophages, or the PE-labeled CD11b (BioLegend, Cat no. 101208) and the Brilliant Violet 421-labeled CD206 antibodies (BioLegend, Cat no.141717) for M2 macrophages, and analyzed by flow cytometry.

2.14. In vivo biodistribution

To prove the gelling of Pluronic hydrogel after injection into mice, the 20 % Pluronic solution (loaded with Rhodamine B, a red dye for visualization) was injected to the mammary pat of a mouse. The mouse was then euthanized, and the injection site was exposed to show whether the Pluronic solution gelled.

To establish a breast cancer model, 4T1 cells were inoculated under the second left nipple of female BALB/c mice (1×10^6 cells/mouse). When the tumor volumes reached 50–100 mm^3, 100 μL of aqueous solution or 20 % Pluronic F127 hydrogels containing FITC-CAT@$CaCO_3$ NPs were intratumorally injected. The *in vivo* imaging system (IVIS) spectrum (PerkinElmer) was used to capture the fluorescent images. Images of mice was taken at 2, 4, 8 and 12 h after the injection.

2.15. Intratumoral pH

The 4T1 triple-negative breast cancer (TNBC) mouse model was established as described above. When the tumor volumes reached 50–100 mm^3, 100 μL of PBS or 20 % Pluronic F127 hydrogels containing catalase, $CaCO_3$ NPs, or CAT@$CaCO_3$ NPs (10 mg/kg mouse, the concentration of $CaCO_3$ NPs was calculated based on the loading efficiency of catalase, termed as CAT-gel, $CaCO_3$ NPs-gel, and CAT@$CaCO_3$ NPs-gel, respectively) was intratumorally injected. The injections were performed twice with a 48-h interval. 24 h after the second injections, 1 nmol of SNARF-4F in 200 μL of PBS was intratumorally injected. Mice were euthanized 20 min after the intratumoral injections to harvest the tumors. All the tumors were cut in half and imaged with IVIS Spectrum.

2.16. Intratumoral ROS level and HIF-1α expression

The 4T1 TNBC mouse model was established as described above. When the tumor volumes reached 50–100 mm^3, 100 μL of PBS, CAT-gel, $CaCO_3$ NPs-gel, or CAT@$CaCO_3$ NPs-gel (catalase 10 mg/kg mouse, the concentration of $CaCO_3$ NPs was calculated based on the loading efficiency of catalase) was intratumorally injected. The injections were performed twice with a 48-h interval. Tumors were extracted 24 h after the second injections and the frozen sections were prepared. The sections were stained with H_2DCFDA for ROS level evaluation or stained with HIF-1α primary antibody (NOVUS, Cat no. NB100-654) and the corresponding fluorescent secondary antibody (Invitrogen, fluorescein-labeled, Cat no. F2765) for HIF-1α detection.

Tumor tissues were also shredded and homogenized. The tissue homogenate was lysed and centrifugated at 12000 g for 10 min to obtain the supernatant containing the proteins. The protein samples from the tumor tissues were separated using SDS-PAGE. HIF-1α and β-tubulin were stained with corresponding primary antibodies (HIF-1α: NOVUS, Cat no. NB100-654; β-tubulin: Invitrogen, Cat no. PA5-16863) and the secondary antibody (Invitrogen, HRP-labeled, Cat no. 65–1620) and shown on the films.

2.17. Anti-tumor effect in orthotopic models

The 4T1 TNBC mouse model was established as described above. When the tumor volumes reached 50–100 mm^3, mice were randomly divided into 5 groups. 100 μL of PBS, CAT-gel, $CaCO_3$ NPs-gel, CAT@$CaCO_3$ NPs-gel, 20 % Pluronic F127 hydrogels containing aPD-1 (termed as aPD-1-gel), or CAT@$CaCO_3$ NPs with aPD-1 (termed as CAT@$CaCO_3$ NPs& aPD-1-gel) (catalase 10 mg/kg mouse, the concentration of $CaCO_3$ NPs was calculated based on the loading efficiency of catalase, aPD-1 150 μg/mouse) was intratumorally injected. Six injections per mouse were given every two days. Tumor volumes and body weights of the mice were recorded. Two days after the last injections, blood was collected from mice and then the mice were euthanized. After euthanasia, the tumors were extracted and weighed and used for immunological analyses. The livers, spleens, kidneys, lungs, and hearts were collected for paraffin sections and hematoxylin and eosin (H&E) staining.

2.18. Anti-tumor effect in distant models

To establish the distant 4T1 TNBC mouse models, 4T1 cells were inoculated under both the second left and right nipples of female BALB/c mice (1×10^6 cells/site) [56]. When the tumor volumes reached 50–100 mm^3, mice were randomly divided into 2 groups. 100 μL of PBS or CAT@$CaCO_3$ NPs& aPD-1-gel (catalase 10 mg/kg mouse, aPD-1 150

μg/mouse) was intratumorally injected into the left-side tumors (designated as the "primary tumors"). The right-side tumors remained untreated (designated as the "distant tumors"). Six injections per mouse were given every two days. Tumor volumes and body weights of the mice were recorded. Two days after the last injections, blood was collected from mice and then the mice were euthanized. After euthanasia, the tumors were extracted and weighed and used for immunological analyses.

2.19. Immunological analyses

The collected tumors were shredded and ground on the cell strainers to harvest cells from the tumors after digestion in the enzyme solution (collagenase IV 2 mg/mL and deoxyribonuclease (DNase) I 0.2 mg/mL). In the case of distant tumor models, the cells in the blood were also isolated after lysis of red blood cells. The cells from blood and tumors were incubated with antibodies for various cell analyses using flow cytometry. The applied antibodies were listed below.

CRT exposure: CRT primary antibody (Invitrogen, Cat no. PA3-900) and the corresponding fluorescent secondary antibody (Invitrogen, Alexa Fluor 555-labeled, Cat no. A21428); All immune cells: CD45 (BioLegend, fluorescein isothiocyanate (FITC)-labeled, Cat no. 103108); DC maturation: CD11c (BioLegend, APC-labeled, Cat no. 117310), CD80 (BioLegend, Pacific Blue-labeled, Cat no. 104724), CD86 (BioLegend, PE-labeled, Cat no. 105008); T cells activation and infiltration: CD3 (BioLegend, Pacific Blue-labeled, Cat no.100214), CD4 (BioLegend, APC-labeled, Cat no.100412), CD8 (BioLegend, PE-labeled, Cat no. 140408); M2 macrophages: F4/80 (BioLegend, APC-labeled, Cat no. 123116), CD11b (BioLegend, PE-labeled, Cat no. 101208), CD206 (BioLegend, Brilliant Violet 421-labeled, Cat no. 141717); M1 macrophages: F4/80 (BioLegend, APC-labeled, Cat no. 123116), CD11b (BioLegend, PE-labeled, Cat no. 101208), CD80 (BioLegend, Pacific Blue-labeled, Cat no. 104724); Treg: CD3 (BioLegend, Pacific Blue-labeled, Cat no. 100214), CD4 (BioLegend, APC-labeled, Cat no.100412), Foxp3 (BioLegend, PE-labeled, Cat no.126404); MDSC: CD11b (BioLegend, PE-labeled, Cat no. 101208), Gr-1 (BioLegend, APC-labeled, Cat no. 108412).

The frozen sections of the tumor tissues were prepared. The sections were stained with CRT (Invitrogen, Cat no. PA3-900) or HMGB1 primary antibody (Invitrogen, Cat no. PA5-27378) and the fluorescent secondary antibody (Invitrogen, Alexa Fluor 555-labeled, Cat no. A21428). The fluorescent images were captured using LSCM(Observer. Z1, Zeiss). The fluorescent intensities of CRT and HMGB1 were quantified using ImageJ software.

The levels of cytokines were also analyzed. 0.3 g of tumor tissues were shredded and homogenized. The tissue homogenate was lysed and centrifugated at 12000 g for 10 min to obtain the supernatant. Similarly, serum from the blood in mice was also collected. The supernatant and serum were used to detect the levels of interferon (IFN)-γ, tumor necrosis factor (TNF)-α, IL-6, IL-10, and IL-12 using enzyme-linked immunosorbent assay (ELISA) kits: IFN-γ (BioLegend, Cat no. 430801), TNF-α (BioLegend, Cat no. 430901), IL-6 (BioLegend, Cat no. 431301), IL-10 (BioLegend, Cat no. 431411), and IL-12 (BioLegend, Cat no. 433604).

2.20. Statistical analysis

All results were presented as mean values ± standard error of the mean. Tukey post-hoc tests and one-way analysis of variance (ANOVA) were used for multiple comparisons. Student's t-test was used for two-group comparisons. All statistical analyses were carried out with Prism software package. The threshold for statistical significance was $p < 0.05$.

3. Results

3.1. Characterizations of CAT@$CaCO_3$ NPs and TME remodeling in vitro

CAT@$CaCO_3$ NPs was prepared *via* co-precipitation method and stabilized with PBLA-PEG [57,58]. L-aspartate acid in PBLA can provide the complexing sites to Ca^{2+} for nucleation and growth and offer steric hindrance to improve the colloidal stability and dispersibility of the nanoparticles [59–63]. The size of CAT@$CaCO_3$ NPs was 187 ± 26 nm at pH 7.4 with and without H_2O_2 by dynamic light scattering (DLS; Fig. 2A), while it decreased to ~40 nm at pH 6.5, a pH miming TME acidity [20,64,65], suggesting that $CaCO_3$ NPs remained stable in H_2O_2 solution but can be degraded gradually in the acidic tumor microenvironment. The response to acidic and/or ROS environment of CAT@$CaCO_3$ NPs was also implied by the changes of zeta-potentials of NPs, which were negative in either pH 7.4 or in H_2O_2 solutions but was reversed to the positive charge in acidic environment (Fig. 2B). This pH responsiveness was also confirmed by morphological changes of CAT@$CaCO_3$ NPs. As shown in Fig. 2C, illustrating the size of CAT@$CaCO_3$ NPs and the breaking apart of CAT@$CaCO_3$ NPs in acidic environment. However, NP size remained unchanged in H_2O_2 solution, indicating that H_2O_2 did not influence the structure of CAT@$CaCO_3$ NPs. The catalase loading level in $CaCO_3$ NPs was ~4.0 %.

Taking advantage of pH responsiveness of $CaCO_3$ NPs, we studied whether $CaCO_3$ NPs can effectively consume protons and elevate or normalize pH to 7.4. Encouraging, it was observed that in the acidic solution (pH 6.5), both $CaCO_3$ NPs and CAT@$CaCO_3$ NPs neutralized the pH of the solutions (Fig. 2D). We then investigate the enzymatic activity of CAT in CAT@$CaCO_3$ NPs. In the H_2O_2 solution, catalase and CAT@$CaCO_3$ NPs effectively scavenged the H_2O_2 (Fig. 2E) and generated O_2 (Fig. 2F). The relief of hypoxia by CAT@$CaCO_3$ NPs was further confirmed by the decreased expression of the HIF-1α in cells treated with CAT@$CaCO_3$ NPs (Fig. 2G and H, S2 and S3), as HIF-1α is stable under hypoxic conditions while degraded in normoxic environments [66]. Hence, CAT@$CaCO_3$ NPs possessed excellent abilities to normalize pH, degrade ROS and relieve hypoxia, and these abilities were in a positive relation with the concentration of CAT@$CaCO_3$ NPs (Fig. S4).

CAT@$CaCO_3$ NPs exhibited a pH dependent release profile, where CAT was released faster in acidic conditions (Fig. 2I and S5), which also indicated pH-responsiveness of $CaCO_3$ NPs. It was also speculated $CaCO_3$ NPs can prevent CAT from rapid degradation *in vivo*, thus maximizing the catalytic activity of CAT. As shown in Fig. 2J, it was found that CAT in CAT@$CaCO_3$ NPs maintained robust catalytic ability in degrading H_2O_2 in the presence of protease K, while CAT alone was quickly degraded. Although the catalytic ability of CAT decreased due to the gradual release of CAT from CAT@$CaCO_3$ NPs in acidic condition, it was still significantly higher than of CAT alone, emphasizing the importance of $CaCO_3$ NPs as the vehicle to deliver catalase.

3.2. CAT@$CaCO_3$ NPs-mediated cytotoxicity and DAMPs release and induction of anti-tumor immune response in vitro

As shown in Fig. 3A, 4T1 cells incubated with FITC-tagged CAT@$CaCO_3$ NPs exhibited efficient uptake of $CaCO_3$ NPs. $CaCO_3$ NPs with or without CAT after degradation either in the acidic TME or in endolysosomes released Ca^{2+} and induced Ca^{2+} accumulation (Fig. 3B). Ca^{2+} overload impaired the mitochondria function, which was reflected by the decreased ratio of JC-1 aggregate to monomer in the mitochondria (Fig. 3C) [38,67]. It has been reported that Ca^{2+} overload can induce cell deaths (Fig. S6) and the release of DAMPs from tumor cells, thereby initiating anti-tumor immune response, which was detailed later [39,68,69]. It was worth noting that 4T1 cells incubated with Ca^{2+} solution did not show the intracellular Ca^{2+} accumulation and mitochondrial damage, emphasizing the necessity of employing $CaCO_3$ NPs to lead to calcium overload in cells.

After incubated with CAT@$CaCO_3$ NPs or blank $CaCO_3$ NPs, 4T1 cells

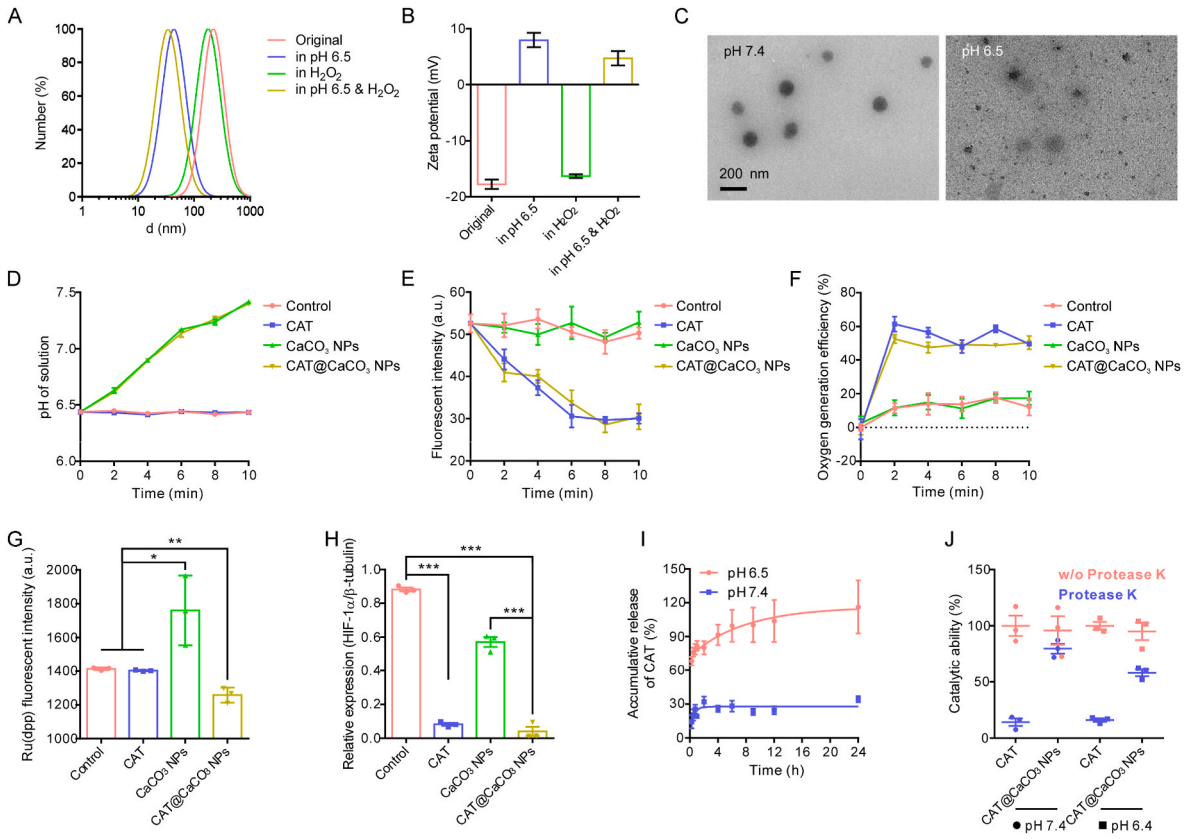

Fig. 2. Characterizations of CAT@$CaCO_3$ NPs and TME remodeling. (A) Particle sizes of CAT@$CaCO_3$ NPs at pH 7.4, pH 6.5, H_2O_2 solution (50 mM) or pH 6.5 with H_2O_2 (50 mM). **(B)** Zeta-potentials of CAT@$CaCO_3$ NPs at pH 7.4, pH 6.5, H_2O_2 solution (50 mM) or pH 6.5 with H_2O_2 (50 mM). **(C)** TEM images of CAT@$CaCO_3$ NPs at pH 7.4 or pH 6.5. **(D)** pH elevation, **(E)** H_2O_2 scavenging, and **(F)** oxygen generation by different formula of NPs in solution. **(G)** Intracellular hypoxia levels in 4T1 cells. The fluorescent intensity of Ru (dpp) is negatively correlated with oxygen levels. **(H)** Semi-quantitative analyses of Western blot analyses of HIF-1α and β-tubulin in 4T1 cells. **(I)** *In vitro* CAT releasing profiles from CAT@$CaCO_3$ NPs at pH 7.4 or pH 6.5. **(J)** Catalytic abilities of CAT and CAT@$CaCO_3$ NPs with or without the presence of protease at pH 7.4 or pH 6.5. *p < 0.05, **p < 0.01, ***p < 0.005. n = 3. Data are presented as mean ± standard error of the mean. Statistical significance was calculated *via* ANOVA with a Tukey post hoc test for multiple comparisons. a.u., arbitrary unit.

exhibited increased exposure of CRT on the surface of cell membrane (Fig. 3D), the secretion of ATP (Fig. 3E), and the release of HMGB1 from nuclear to cytosol (Fig. 3F and S7). These DAMP signals and the simultaneously released TAAs can maturate DC and can be processed to T cells by the maturated DC to elicit the immune responses [70–74].

As demonstrated earlier that CAT@$CaCO_3$ NPs can normalizing pH, ROS level, and O_2 levels in TME, we studied whether these changes would influence the activity or phenotypes of immune cells. CAT@$CaCO_3$ NPs-treated 4T1 cells significantly elevated the percentage of mature DCs ($CD80^+CD86^+$ in $CD11c^+$; Fig. 3G) compared with control, free catalase. Furthermore, CAT@$CaCO_3$ NPs treatment led to the polarization of macrophages from the anti-inflammatory M2 phenotype to the pro-inflammatory M1 (Fig. 3H). M1 macrophages can express major histocompatibility complex class II for antigen presentation [75–77].

3.3. CAT@$CaCO_3$ NPs for TME remodeling in vivo

Biodistribution of intratumorally injected CAT@$CaCO_3$ NPs was evaluated. To prolong the retention of NPs in tumor tissues, we exploited the injectable Pluronic hydrogel. Pluronic hydrogel possesses the advantages including the excellent biocompatibility, injectability, and thermos-sensitivity (remaining the liquid state at room temperature but gelling at body temperature, Fig. S8A), which has been applied in many studies including for intratumoral injections [78–82]. FITC-CAT@$CaCO_3$ NPs in Pluronic hydrogel were injected into 4T1 TNBC tumors. CAT@$CaCO_3$ NPs in hydrogels showed significant longer tumor retention (Fig. S8B).

SNARF-4F, the indicator of the intratumoral pH change, undergoes a pH-dependent fluorescence emission swift [83–85]. Thus, the elevated ratio of fluorescent intensities at 640 nm–580 nm indicates the pH elevation. As illustrated in Fig. 4A and B, tumors treated with $CaCO_3$ NPs-gel and CAT@ $CaCO_3$ NPs-gel exhibited higher ratios than control and CAT-gel groups, indicating that the intratumorally injected $CaCO_3$ NPs elevated the pH in tumor tissues. ROS levels in TME were shown in Fig. 4C and D. Lower ROS levels were found in CAT-gel and CAT@$CaCO_3$ NPs-gel groups. Furthermore, HIF-1α expression in tumor tissues were investigated (Fig. 4E–G and S9). Lower expression of HIF-1α was also detected in both CAT-gel and CAT@$CaCO_3$ NPs-gel groups, indicating that CAT effectively relieved the hypoxic microenvironment in tumor tissues. All these results supported that CAT@$CaCO_3$ NPs treatment can successfully remodel the TME, providing an advantageous environment for the activation of anti-tumor immunity.

3.4. CAT@$CaCO_3$ NPs treatment for inhibition of tumor growth

The anti-tumor efficacy of CAT@$CaCO_3$ NPs was evaluated on the orthotopic 4T1 TNBC mouse model. Saline (as the control), CAT-gel, $CaCO_3$ NPs-gel, or CAT@$CaCO_3$ NPs-gel was intratumorally injected (Fig. S10A). CAT@$CaCO_3$ NPs-gel exhibited the best control of tumor growth compared with control, CAT-gel, and $CaCO_3$ NPs-gel groups (Fig. 5A and B and S10B). No change in body weights was observed in treatment groups (Figs. S10C and S10D), and the H&E analyses of hearts, livers, spleens, lungs and kidneys showed no obvious toxicity to the major organs (Fig. 5C), which confirmed the excellent

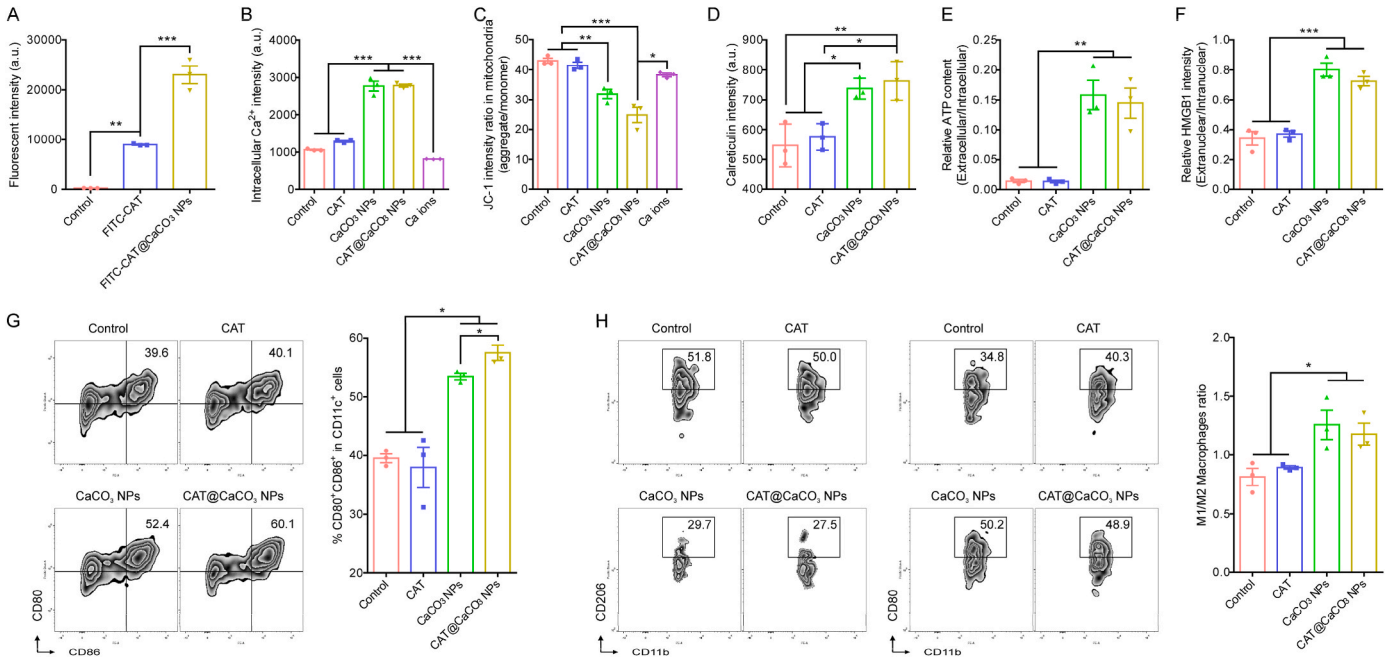

Fig. 3. CAT@$CaCO_3$ NPs-mediated DAMPs release and induction of anti-tumor immune response *in vitro*. **(A)** Cellular uptake of CAT and CAT@$CaCO_3$ NPs by 4T1 cells. **(B)** Intracellular Ca^{2+} levels and **(C)** mitochondrial damage in 4T1 cells. **(D)** Intensity of surface-exposed CRT, **(E)** relative ATP content, and **(F)** relative HMGB1 intensity in 4T1 cells. **(G)** Flow cytometry analyses of matured DCs ($CD80^+CD86^+$ in $CD11c^+$) after NP treatment. **(H)** Flow cytometry analyses of M2 macrophages ($CD11b^+CD206^+$) and M1 macrophages ($CD11b^+CD80^+$). *p < 0.05, **p < 0.01, ***p < 0.005. n = 3. Data are presented as mean ± standard error of the mean. Statistical significance was calculated *via* ANOVA with a Tukey post hoc test for multiple comparisons. a.u., arbitrary unit.

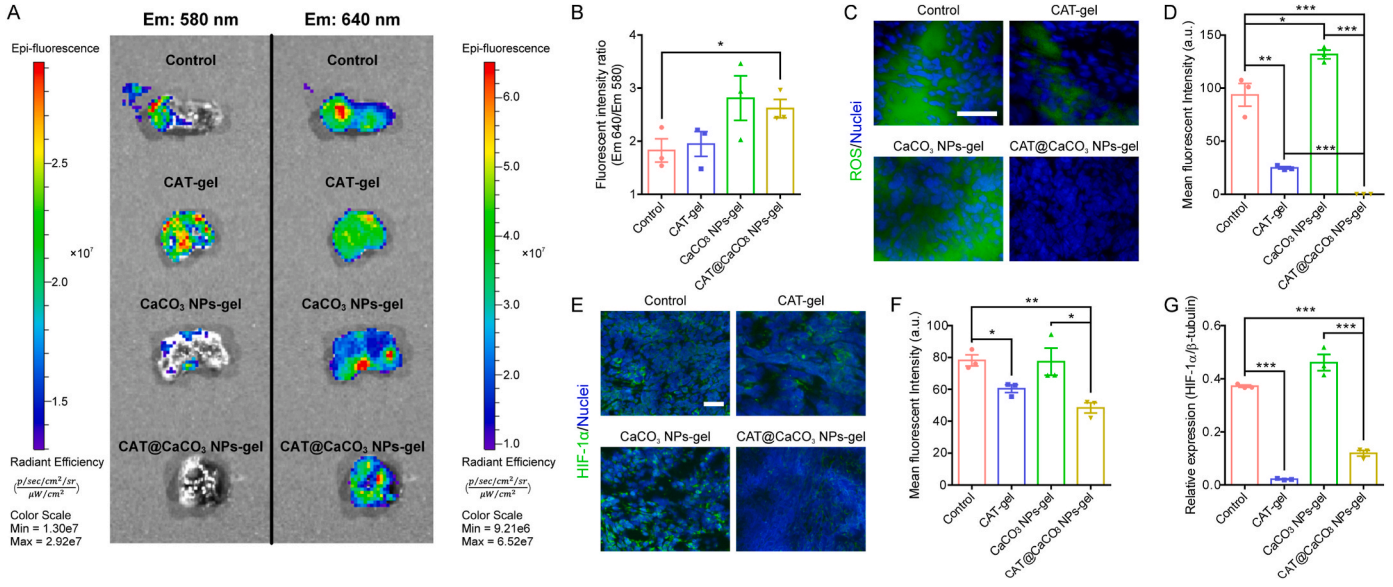

Fig. 4. CAT@$CaCO_3$ NPs for TME remodeling *in vivo*. **(A)** IVIS images of tumors and **(B)** the ratio of fluorescent intensities at Em 640 nm–580 nm indicating pH in TME after receiving intratumoral injections. The elevated ratio of fluorescent intensities at 640 nm–580 nm indicates the pH elevation. **(C)** LSCM images and **(D)** semi-quantitative analyses of ROS levels in tumor tissue after different treatments. **(E)** LSCM images and **(F)** semi-quantitative analyses of HIF-1α expression in frozen sections of tumors after different treatments. **(G)** Semi-quantitative analyses of the Western blot analysis of HIF-1α and β-tubulin in tumors after different treatments. Scale bar, 50 μm *p < 0.05, **p < 0.01, ***p < 0.005. n = 3. Data are presented as mean ± standard error of the mean. Statistical significance was calculated *via* one-way ANOVA with a Tukey post hoc test for multiple comparisons. a.u., arbitrary unit.

biocompatibility of CAT@$CaCO_3$ NPs.

Tumor tissues were collected for immunological analyses. The increased CRT exposure on tumor cells and the release of HMGB1 from nucleus to cytosol were observed in $CaCO_3$ NPs-treated groups (Figs. S11 and S12A). An elevated level of DC maturation ($CD80^+CD86^+$ in $CD11c^+$; Fig. 5D) and anti-tumor immune activation ($CD45^+$; Fig. 5E and S12K) were shown in the CAT@$CaCO_3$ group. CAT@$CaCO_3$ NPs treatment also led to efficient polarization of tumor-associated macrophages from the immune-suppressive M2 phenotype ($F4/80^+CD206^+$; Figs. S12B and S12N) to the immune-supportive M1 phenotype ($F4/80^+CD80^+$; Fig. 5I, S12C and S12M). Furthermore, the number of tumor-infiltrating lymphocytes (TIL; $CD3^+$; Fig. 5F) increased in CAT@$CaCO_3$ NPs-treated tumors, where the highest percentages of helper T lymphocytes ($CD3^+CD4^+$; Fig. 5G and S12L) and cytotoxic T lymphocytes

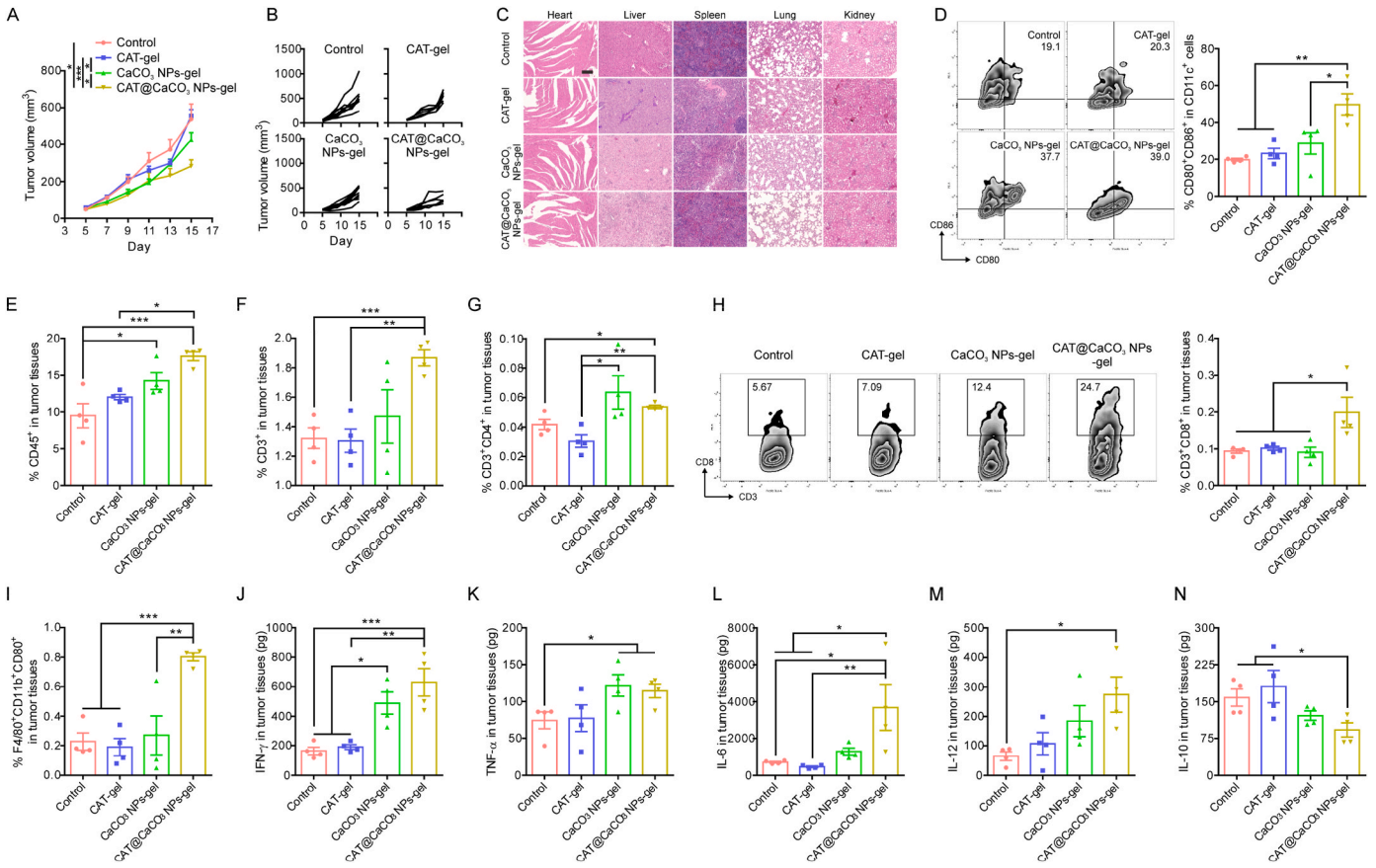

Fig. 5. ***In vivo*** **antitumoral effect of CAT@$CaCO_3$ NPs on the orthotopic tumor model. (A)** Average and **(B)** individual tumor growth kinetics in different groups (n = 7–10). **(C)** H&E-stained sections of hearts, kidneys, livers, lungs, and spleens from TNBC-bearing mice after treatment. Scale bar, 500 μm. **(D)** Flow cytometry analysis of matured DCs ($CD80^+CD86^+$ in $CD11c^+$). Percentages of **(E)** all immune cells ($CD45^+$), **(F)** TIL ($CD3^+$) and **(G)** $CD4^+$ T cells ($CD4^+CD3^+$) in tumors. **(H)** Flow cytometry analysis of $CD8^+$ T cells ($CD8^+$ in $CD3^+$) in tumors. **(I)** Percentages of M1 macrophages ($F4/80^+CD80^+$) in tumors. Levels of **(J)** IFN-γ and **(K)** TNF-α, **(L)** IL-6, **(M)** IL-12, and **(N)** IL-10 in 50 mg tumor tissues. *p < 0.05, **p < 0.01, ***p < 0.005. n = 4. Data are presented as mean ± standard error of the mean. Statistical significance was calculated *via* one-way ANOVA with a Tukey post hoc test for multiple comparisons.

($CD3^+CD8^+$; Fig. 5H) were also observed. Meanwhile, Tregs ($CD3^+CD4^+Foxp3^+$; Figs. S12D–F and S12O), the immunosuppressive T cells in the TME, significantly decreased after in the CAT@$CaCO_3$ NPs group. In addition, the number of immunosuppressive MDSCs ($CD11b^+Gr\text{-}1^+$; Figs. S12G and S12P) was also significantly decreased induced by CAT@$CaCO_3$ NPs. The intratumoral levels of cytokines were detected by ELISA. The highest levels of IFN-γ (Fig. 5J), TNF-α (Fig. 5K), IL-6 (Fig. 5L), and IL-12 (Fig. 5M), the pro-inflammatory cytokines, and the lowest concentration of IL-10 (Fig. 5N), an anti-inflammatory cytokine, were all detected in CAT@$CaCO_3$ NPs-treated tumor tissues. Besides, T cells in blood were also analyzed. CAT@$CaCO_3$ NPs displayed the highest percentages of $CD3^+$ T cells TIL (Fig. S12H), including both helper T lymphocytes and cytotoxic T lymphocytes (Figs. S12I and S12J and S12Q), suggesting that local CAT@$CaCO_3$ NPs treatment can awaken the systemic anti-immune immunity for treating potential metastatic disease. These immunological analysis results revealed that CAT@$CaCO_3$ NPs can effectively activate the anti-tumor immunity by increasing and activating immune-supportive cells (i.e., mature DC, T lymphocytes, and M1 TAM) and decreasing the immunosuppressive cells (i.e., M2 TAM, Treg, MDSC), thereby providing clear rationale to combine CAT@$CaCO_3$ NPs with immune checkpoint inhibitors, such as aPD-1, to further enhance T-cell mediated anti-tumor efficacy.

Therefore, the anti-tumor efficacy of combining CAT@$CaCO_3$ NPs and aPD-1 antibody was investigated. Saline (as the control), CAT@-$CaCO_3$ NPs-gel, aPD-1-gel, or CAT@$CaCO_3$ NPs&aPD-1-gel was intratumorally injected (Fig. S13A). Expectedly, this combination treatment further inhibited the tumor growth compared to CAT@$CaCO_3$ NPs (Fig. 6A and B and Fig. S13B). No obvious toxicity of the injections was reflected by the constant body weight (Figs. S13C and S13D) and healthy tissues in major organs (hearts, livers, spleens, lungs and kidneys) in the H&E-stained sections (Fig. S13E). Immunological analysis was also conducted (Fig. 6C–K and S14). The percentages of TIL (Fig. 6C), including helper T lymphocytes (Fig. 6D and S14O) and cytotoxic T lymphocytes (Fig. 6E), were significantly elevated in the combination groups. Similar trends were also found in T cells in blood (Fig. S14J-L and S14T). It was also observed that the combination treatment further promoted the polarization of TAMs from M2 phenotype to M1 phenotype (Fig. 6F, S14D, S14E, S14P and S14Q) and the decrease of Treg cells (Figs. S14F–H and S14R) and MDSC (Figs. S14I and S14S) in tumor tissues. In terms of cytokines, the combination group further promoted the secretion of IFN-γ (Fig. 6G), TNF-α (Fig. 6H), IL-6 (Fig. 6I), and IL-12 (Fig. 6J, the pro-inflammatory cytokines, and declined the level of IL-10 (Fig. 6K), the anti-inflammatory cytokine, compared with CAT@$CaCO_3$ NPs.

3.5. *The combination of CAT@$CaCO_3$ NPs and aPD-1 for treating distant tumors*

After confirming that the combination of CAT@$CaCO_3$ NPs and aPD-1 can effectively activate the local anti-tumor immunity, we investigated whether this local treatment can activate the systemic immunity to combat distant tumors. Mice were inoculated with two separated 4T1 tumors as described as a simplified distant tumor model for experiments [86,87]. The left-side tumors received CAT@$CaCO_3$ NPs&aPD-1

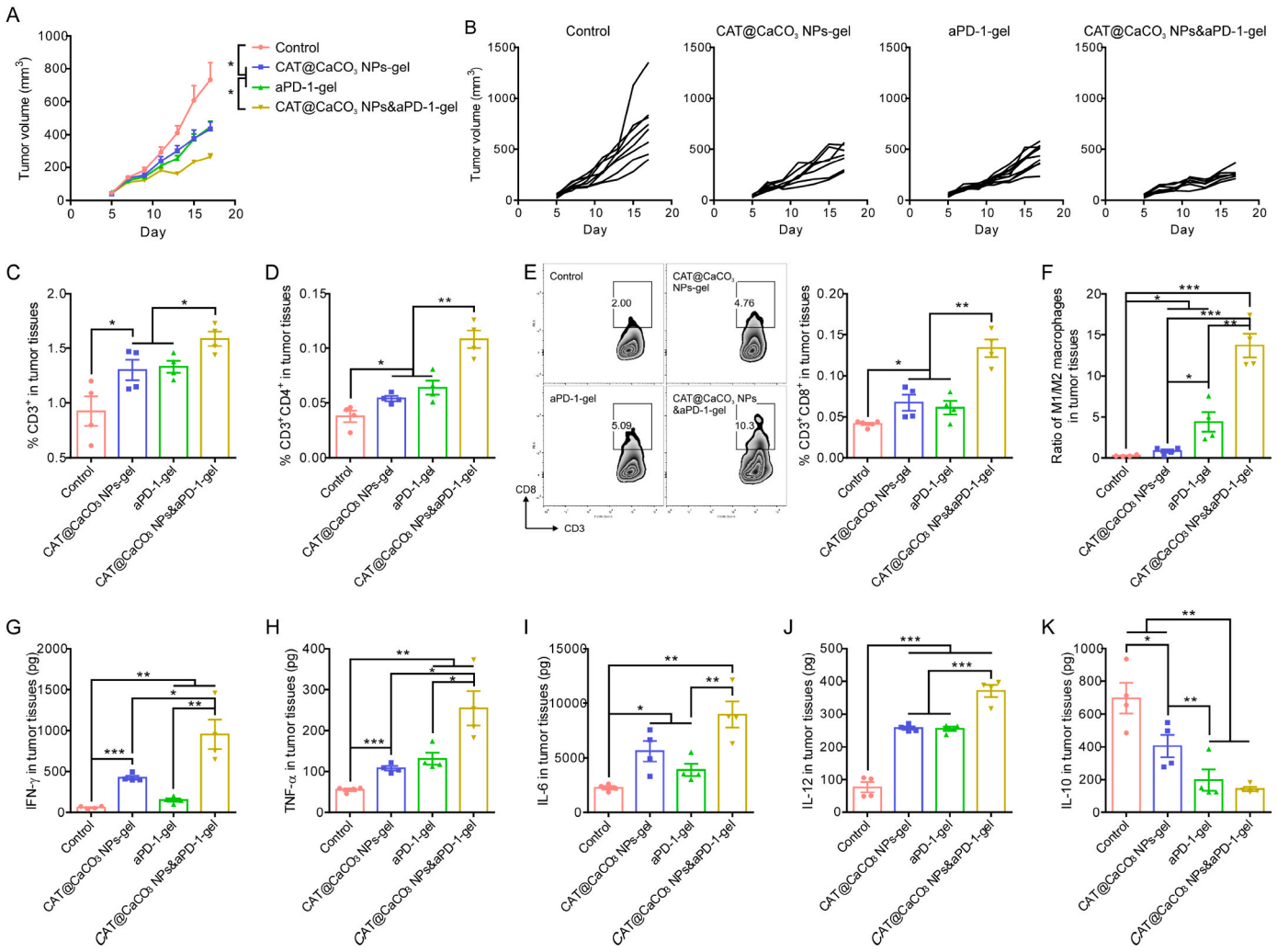

Fig. 6. ***In vivo*** **antitumoral effect of CAT@$CaCO_3$ NPs combined with aPD-1.** **(A)** Average and **(B)** individual tumor growth kinetics in different groups (n = 7–10). **(C)** Percentages of TIL ($CD3^+$) and **(D)** $CD4^+$ T cells ($CD4^+CD3^+$) in tumors. **(E)** Flow cytometry analysis of $CD8^+$ T cells ($CD8^+$ in $CD3^+$) in tumors. **(F)** Ratio of M1 ($F4/80^+CD80^+$) to M2 macrophages ($F4/80^+CD206^+$). Levels of **(G)** IFN-γ, **(H)** TNF-α, **(I)** IL-6, **(J)** IL-12, and **(K)** IL-10 in 50 mg tumor tissues. *p < 0.05, **p < 0.01, ***p < 0.005. n = 4. Data are presented as mean ± standard error of the mean. Statistical significance was calculated *via* one-way ANOVA with a Tukey post hoc test for multiple comparisons.

treatment while the right-side tumors remained untreated (Fig. S15A). local CAT@$CaCO_3$ NPs&aPD-1 treatment on one tumor exhibited robust efficacy in inhibiting tumor growth of untreated tumors (Fig. 7A and B and Fig. S15B). The immunological profiling on primary and distant tumors as well as blood was evaluated (Fig. 7C-Q and S16). The numbers of immune cells in both primary and distant tumors significantly increased in the treated group (Fig. 7C and S16F). The numbers of the immune-supportive cells, including TIL (Fig. 7D), $CD4^+$ T cells (Fig. 7F and S16F), $CD8^+$ T cells (Fig. 7E), and M1 macrophages (Fig. 7G and S16H) were elevated, while the percentages of immunosuppressive cells like M2 macrophages (Fig. 7H, S16A and S16I), Tregs (Figs. S16B-D and S16J), and MDSC (Figs. S16E and S16K) decreased in both primary and distant tumors in the treated group, indicating that the anti-tumor immunity was also effectively activated in distant tumor areas after the local treatment of primary tumors. The evident elevation of TIL, $CD4^+$ T cells and $CD8^+$ T cells was observed in the blood in the treated group (Fig. 7I-L), demonstrating that the systemic anti-tumor immunity was successfully activated. Additionally, the obvious increase in the levels of pro-inflammatory cytokines, including IFN-γ (Fig. 7M and S16L), TNF-α (Fig. 7N and S16M), IL-6 (Fig. 7O and S16N) and IL-12 (Fig. 7P and S16O), and the decline of anti-inflammatory IL-10 (Fig. 7Q and S16P) were detected in the treated animals.

4. Discussion

In this article, we reported a TME-responsive and immunotherapeutic CAT@$CaCO_3$ NP as a simple and versatile multi-modulator to remodel TME for enhanced ICB therapy. Specifically, $CaCO_3$ NPs effectively consumed the excessive protons in the acidic TME to normalize the TEM pH. CAT catalyzed the decomposition of ROS rich in the TME and generated oxygen, thereby simultaneously decreasing ROS levels and relieving hypoxia in the TME. Meanwhile, Ca^{2+} released from $CaCO_3$ NPs caused Ca^{2+}-mediated DAMP release, thereby initiating effective antigen presentation by DCs. Moreover, the immunosupportive TME shaped by CAT@$CaCO_3$ NPs promoted the polarization of TAMs to the M1 phenotype, further facilitating tumor antigen presentation. Consequently, T-cell-mediated anti-tumor immune responses were then activated and further augmented by aPD-1 therapy. The local treatment of the combined CAT@$CaCO_3$ NPs and aPD-1 exhibited significant control of tumor growth of both treated (or primary) and untreated (or 'distant') tumors, proving that this is a promising therapeutic method for enhancing cancer immunotherapy.

While these results underscore clinical potential of this strategy, several considerations warrant exploration in future investigations. Firstly, the intratumoral delivery of the treatment, while feasible for

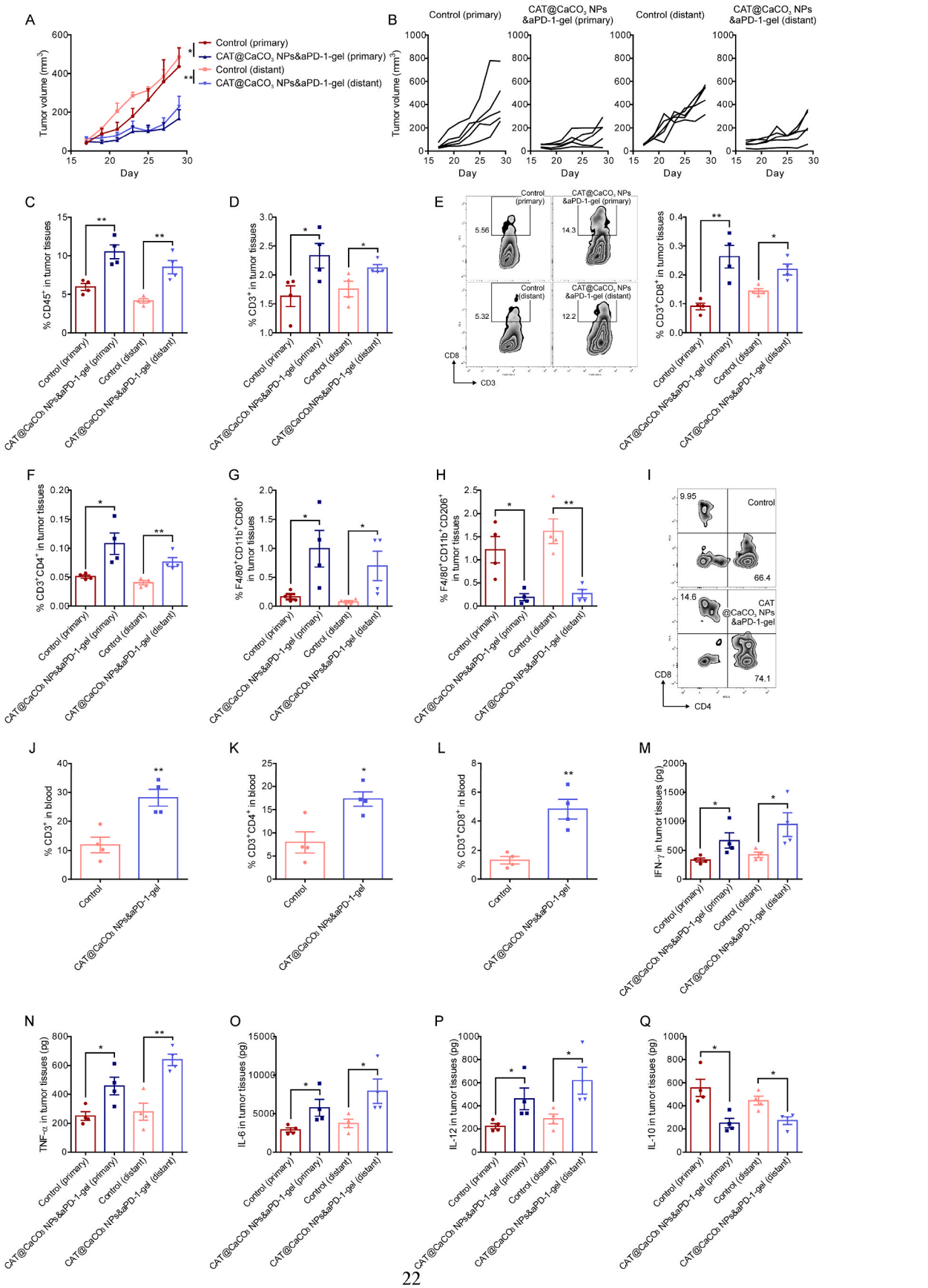

(caption on next page)

Fig. 7. ***In vivo*** **antitumoral effect of CAT@$CaCO_3$ NPs combined with aPD-1 on the distant tumor model.** **(A)** Average and **(B)** individual tumor growth kinetics in different groups (n = 5). Percentages of **(C)** all immune cells ($CD45^+$) and **(D)** TIL ($CD3^+$). **(E)** Flow cytometry analysis of $CD8^+$ T cells ($CD8^+$ in $CD3^+$) in tumors. Percentages of **(F)** $CD4^+$ T cells ($CD4^+CD3^+$), **(G)** M1 macrophages ($F4/80^+CD80^+$) and **(H)** M2 macrophages ($F4/80^+CD206^+$) in tumors. **(I)** Flow cytometry analysis of $CD4^+$ T cells ($CD4^+$ in $CD3^+$) and $CD8^+$ T cells ($CD8^+$ in $CD3^+$) in blood. Percentages of **(J)** TIL ($CD3^+$), **(K)** $CD4^+$ T cells ($CD3^+CD4^+$) and **(L)** $CD8^+$ T cells ($CD3^+CD8^+$) in blood. Levels of **(M)** IFN-γ, **(N)** TNF-α, **(O)** IL-6, **(P)** IL-12, and **(Q)** IL-10 in 50 mg tumor tissues. *$p < 0.05$, **$p < 0.01$. n = 4. Data are presented as mean ± standard error of the mean. Statistical significance was calculated *via* one-way ANOVA with a Tukey post hoc test for multiple comparisons, *via* Student's t-test for two-group comparisons.

superficial tumors like TNBC or melanoma, may require optimization for deeper tissue and organ tumors (e.g., liver, brain, and colon) that are not as easily amenable to intratumoral injections, although image-guided intratumoral approaches are possible [88–90]. Secondly, the effectiveness of this combination strategy should be further assessed in more advanced preclinical models, such as patient-derived xenograft humanized mouse models and/or larger animal models, necessitating potential adjustments to the treatment regimen. Thirdly, given the variability in immune cell profiling within TME across different tumor models, exploring the combination of CAT@$CaCO_3$ NPs with appropriately selected immune checkpoint inhibitors becomes imperative. Lastly, the integration of strategies to overcome other physical barriers within the TME, such as the dense extracellular matrix [15,91–93], presents a promising avenue for further enhancement.

Funding

The start-up package from McGill University (G.C.)
CIHR grants (G.C.)
CCS-Challenge Grants (G.C.)

Ethics approval and consent to participate

All animal-related experiments were carried out following the animal protocol approved by McGill University.

CRediT authorship contribution statement

Tianxu Fang: Conceptualization, Formal analysis, Investigation, Writing – original draft, Writing – review & editing. **Xiaona Cao:** Investigation. **Li Wang:** Investigation. **Mo Chen:** Investigation. **Yueyang Deng:** Investigation. **Guojun Chen:** Conceptualization, Funding acquisition, Investigation, Project administration, Resources, Supervision, Writing – original draft, Writing – review & editing.

Declaration of competing interest

The authors declare no conflict of interest.

Acknowledgments

This work was supported by the start-up package from McGill University (to G.C.), CIHR grants (to G.C.), and CCS-Challenge Grants (to G.C.). T.F. would also like to acknowledge the Rolande and Marcel Gosselin Graduate Studentship, Dr. Victor KS Lui Studentship, Charlotte and Leo Karassik Foundation Oncology Ph.D. Fellowship from the Rosalind & Morris Goodman Cancer Institute as well as the BME recruitment award. The authors thank Dr. Peter Siegel at McGill University for providing the 4T1 cell line. The authors also acknowledge the McGill Life Science Complex Flow Cytometry Core, the Histology Core, and the GCI Research Support team.

Appendix A. Supplementary data

Supplementary data to this article can be found online at https://doi.org/10.1016/j.bioactmat.2023.10.023.

References

[1] J.C. Del Paggio, Cancer immunotherapy and the value of cure, Nat. Rev. Clin. Oncol. 15 (5) (2018) 268–270.
[2] S.A. Rosenberg, J.C. Yang, N.P. Restifo, Cancer immunotherapy: moving beyond current vaccines, Nat. Med. 10 (9) (2004) 909–915.
[3] E.I. Buchbinder, F.S. Hodi, Immune-checkpoint blockade—durable cancer control, Nat. Rev. Clin. Oncol. 13 (2) (2016) 77–78.
[4] A. Kalbasi, A. Ribas, Tumour-intrinsic resistance to immune checkpoint blockade, Nat. Rev. Immunol. 20 (1) (2020) 25–39.
[5] T. Tang, X. Huang, G. Zhang, Z. Hong, X. Bai, T. Liang, Advantages of targeting the tumor immune microenvironment over blocking immune checkpoint in cancer immunotherapy, Signal Transduct. Targeted Ther. 6 (1) (2021) 1–13.
[6] M.O. de Olza, B.N. Rodrigo, S. Zimmermann, G. Coukos, Turning up the heat on non-immunoreactive tumours: opportunities for clinical development, Lancet Oncol. 21 (9) (2020) e419–e430.
[7] G. Liu, W. Rui, X. Zhao, X. Lin, Enhancing CAR-T cell efficacy in solid tumors by targeting the tumor microenvironment, Cell. Mol. Immunol. 18 (5) (2021) 1085–1095.
[8] N.M. Anderson, M.C. Simon, The tumor microenvironment, Curr. Biol. 30 (16) (2020) R921–R925.
[9] R. Baghban, L. Roshangar, R. Jahanban-Esfahlan, K. Seidi, A. Ebrahimi-Kalan, M. Jaymand, S. Kolahian, T. Javaheri, P. Zare, Tumor microenvironment complexity and therapeutic implications at a glance, Cell Commun. Signal. 18 (1) (2020) 59.
[10] M. Yang, J. Li, P. Gu, X. Fan, The application of nanoparticles in cancer immunotherapy: targeting tumor microenvironment, Bioact. Mater. 6 (7) (2021) 1973–1987.
[11] Q. Wang, X. Shao, Y. Zhang, M. Zhu, F.X.C. Wang, J. Mu, J. Li, H. Yao, K. Chen, Role of tumor microenvironment in cancer progression and therapeutic strategy, Cancer Med. 12 (10) (2023) 11149–11165.
[12] T.L. Whiteside, The tumor microenvironment and its role in promoting tumor growth, Oncogene 27 (45) (2008) 5904–5912.
[13] Y. Yuan, Y.-C. Jiang, C.-K. Sun, Q.-M. Chen, Role of the tumor microenvironment in tumor progression and the clinical applications, Oncol. Rep. 35 (5) (2016) 2499–2515 (Review).
[14] K. Khalaf, D. Hana, J.T. Chou, C. Singh, A. Mackiewicz, M. Kaczmarek, Aspects of the tumor microenvironment involved in immune resistance and drug resistance, Front. Immunol. 12 (2021), 656364.
[15] Y. Chao, Z. Liu, Biomaterials tools to modulate the tumour microenvironment in immunotherapy, Nat. Rev. Bioeng. 1 (2) (2023) 125–138.
[16] V. Sharma, R. Kaur, A. Bhatnagar, J. Kaur, Low-pH-induced apoptosis: role of endoplasmic reticulum stress-induced calcium permeability and mitochondria-dependent signaling, Cell Stress Chaperones 20 (3) (2015) 431–440.
[17] H. Nakamura, K. Takada, Reactive oxygen species in cancer: current findings and future directions, Cancer Sci. 112 (10) (2021) 3945–3952.
[18] B. Muz, P. de la Puente, F. Azab, A.K. Azab, The role of hypoxia in cancer progression, angiogenesis, metastasis, and resistance to therapy, Hypoxia 3 (2015) 83–92.
[19] S. Uthaman, K.M. Huh, I.K. Park, Tumor microenvironment-responsive nanoparticles for cancer theragnostic applications, Biomater. Res. 22 (2018) 22.
[20] M. Bellone, A. Calcinotto, P. Filipazzi, A. De Milito, S. Fais, L. Rivoltini, The acidity of the tumor microenvironment is a mechanism of immune escape that can be overcome by proton pump inhibitors, OncoImmunology 2 (1) (2013), e22058.
[21] J.X. Wang, S.Y.C. Choi, X. Niu, N. Kang, H. Xue, J. Killam, Y. Wang, Lactic acid and an acidic tumor microenvironment suppress anticancer immunity, Int. J. Mol. Sci. 21 (21) (2020).
[22] A. Kotsafti, M. Scarpa, I. Castagliuolo, M. Scarpa, Reactive oxygen species and antitumor immunity-from surveillance to evasion, Cancers 12 (7) (2020).
[23] B. Wang, Q. Zhao, Y. Zhang, Z. Liu, Z. Zheng, S. Liu, L. Meng, Y. Xin, X. Jiang, Targeting hypoxia in the tumor microenvironment: a potential strategy to improve cancer immunotherapy, J. Exp. Clin. Cancer Res. 40 (1) (2021) 24.
[24] Z. Chen, F. Han, Y. Du, H. Shi, W. Zhou, Hypoxic microenvironment in cancer: molecular mechanisms and therapeutic interventions, Signal Transduct. Targeted Ther. 8 (1) (2023) 70.
[25] A. Sahu, I. Kwon, G. Tae, Improving cancer therapy through the nanomaterials-assisted alleviation of hypoxia, Biomaterials 228 (2020), 119578.
[26] J. Wu, J. Song, X. Yin, J. Tang, J. Zhang, X. Wang, Y. Ji, Y. Zhao, D. Chen, J. Sheng, X. Bai, T. Liang, Recent advancements of nanotechnology-based strategies for overcoming tumor microenvironment hypoxia, Front. Biosci. 27 (5) (2022) 145.
[27] N. Yang, W. Xiao, X. Song, W. Wang, X. Dong, Recent advances in tumor microenvironment hydrogen peroxide-responsive materials for cancer photodynamic therapy, Nano-Micro Lett. 12 (1) (2020) 15.
[28] Q. Jiang, B. Qiao, X. Lin, J. Cao, N. Zhang, H. Guo, W. Liu, L. Zhu, X. Xie, L. Wan, R. Tang, B. Liang, D. Wang, Z. Wang, Y. Zhou, H. Ran, P. Li, A hydrogen peroxide

economizer for on-demand oxygen production-assisted robust sonodynamic immunotherapy, Theranostics 12 (1) (2022) 59–75.
[29] S.Y. Zhai, M.G. Kong, Y.M. Xia, Cold atmospheric plasma ameliorates skin diseases involving reactive oxygen/nitrogen species-mediated functions, Front. Immunol. 13 (2022), 868386.
[30] K. Sklias, J. Santos Sousa, P.M. Girard, Role of short- and long-lived reactive species on the selectivity and anti-cancer action of plasma treatment in vitro, Cancers 13 (4) (2021).
[31] Y. Hei, B. Teng, Z. Zeng, S. Zhang, Q. Li, J. Pan, Z. Luo, C. Xiong, S. Wei, Multifunctional immunoliposomes combining catalase and PD-L1 antibodies overcome tumor hypoxia and enhance immunotherapeutic effects against melanoma, Int. J. Nanomed. 15 (2020) 1677–1691.
[32] X. Song, J. Xu, C. Liang, Y. Chao, Q. Jin, C. Wang, M. Chen, Z. Liu, Self-supplied tumor oxygenation through separated liposomal delivery of H(2)O(2) and catalase for enhanced radio-immunotherapy of cancer, Nano Lett. 18 (10) (2018) 6360–6368.
[33] Z. Tong, Y. Gao, H. Yang, W. Wang, Z. Mao, Nanomaterials for cascade promoted catalytic cancer therapy, View 2 (6) (2021).
[34] P. Zhao, Y. Tian, J. You, X. Hu, Y. Liu, Recent advances of calcium carbonate nanoparticles for biomedical applications, Bioengineering 9 (11) (2022).
[35] Y. Ueno, H. Futagawa, Y. Takagi, A. Ueno, Y. Mizushima, Drug-incorporating calcium carbonate nanoparticles for a new delivery system, J. Contr. Release 103 (1) (2005) 93–98.
[36] D.B. Trushina, T.N. Borodina, S. Belyakov, M.N. Antipina, Calcium carbonate vaterite particles for drug delivery: advances and challenges, Mater. Today Adv. 14 (2022), 100214.
[37] A. Alaimo, M. Lorenzoni, P. Ambrosino, A. Bertossi, A. Bisio, A. Macchia, E. Zoni, S. Genovesi, F. Cambuli, V. Foletto, D. De Felice, M.V. Soldovieri, I. Mosca, F. Gandolfi, M. Brunelli, G. Petris, A. Cereseto, A. Villarroel, G. Thalmann, F. G. Carbone, M. Kruithof-de Julio, M. Barbareschi, A. Romanel, M. Taglialatela, A. Lunardi, Calcium cytotoxicity sensitizes prostate cancer cells to standard-of-care treatments for locally advanced tumors, Cell Death Dis. 11 (12) (2020) 1039.
[38] M. Zhang, R. Song, Y. Liu, Z. Yi, X. Meng, J. Zhang, Z. Tang, Z. Yao, Y. Liu, X. Liu, W. Bu, Calcium-overload-mediated tumor therapy by calcium peroxide nanoparticles, Chem 5 (8) (2019) 2171–2182.
[39] P. Zheng, B. Ding, Z. Jiang, W. Xu, G. Li, J. Ding, X. Chen, Ultrasound-augmented mitochondrial calcium ion overload by calcium nanomodulator to induce immunogenic cell death, Nano Lett. 21 (5) (2021) 2088–2093.
[40] J. An, K. Zhang, B. Wang, S. Wu, Y. Wang, H. Zhang, Z. Zhang, J. Liu, J. Shi, Nanoenabled disruption of multiple barriers in antigen cross-presentation of dendritic cells via calcium interference for enhanced chemo-immunotherapy, ACS Nano 14 (6) (2020) 7639–7650.
[41] B.Q. Chen, Y. Zhao, Y. Zhang, Y.J. Pan, H.Y. Xia, R.K. Kankala, S.B. Wang, G. Liu, A.Z. Chen, Immune-regulating camouflaged nanoplatforms: a promising strategy to improve cancer nano-immunotherapy, Bioact. Mater. 21 (2023) 1–19.
[42] Y. Yang, Y. Zhu, K. Wang, Y. Miao, Y. Zhang, J. Gao, H. Qin, Y. Zhang, Activation of autophagy by in situ Zn(2+) chelation reaction for enhanced tumor chemoimmunotherapy, Bioact. Mater. 29 (2023) 116–131.
[43] Z. Li, H. Cai, Z. Li, L. Ren, X. Ma, H. Zhu, Q. Gong, H. Zhang, Z. Gu, K. Luo, A tumor cell membrane-coated self-amplified nanosystem as a nanovaccine to boost the therapeutic effect of anti-PD-L1 antibody, Bioact. Mater. 21 (2023) 299–312.
[44] F.N. Castellano, J.R. Lakowicz, A water-soluble luminescence oxygen sensor, Photochem. Photobiol. 67 (2) (1998).
[45] S.Y. Zhao, B.S. Harrison, Morphology impact on oxygen sensing ability of Ru(dpp)3Cl2 containing biocompatible polymers, Mater. Sci. Eng., C 53 (2015) 280–285.
[46] R.M. Bukowski, R. Ciriminna, M. Pagliaro, F.V. Bright, High-performance quenchometric oxygen sensors based on fluorinated xerogels doped with [Ru(dpp)3]2+, Anal. Chem. 77 (8) (2005) 2670–2672.
[47] H. Wang, Y. Chao, J. Liu, W. Zhu, G. Wang, L. Xu, Z. Liu, Photosensitizer-crosslinked in-situ polymerization on catalase for tumor hypoxia modulation & enhanced photodynamic therapy, Biomaterials 181 (2018) 310–317.
[48] Y. Zhao, Z. Luo, M. Li, Q. Qu, X. Ma, S.H. Yu, Y. Zhao, A preloaded amorphous calcium carbonate/doxorubicin@silica nanoreactor for pH-responsive delivery of an anticancer drug, Angew Chem. Int. Ed. Engl. 54 (3) (2015) 919–922.
[49] R. Zhang, X. Song, C. Liang, X. Yi, G. Song, Y. Chao, Y. Yang, K. Yang, L. Feng, Z. Liu, Catalase-loaded cisplatin-prodrug-constructed liposomes to overcome tumor hypoxia for enhanced chemo-radiotherapy of cancer, Biomaterials 138 (2017) 13–21.
[50] C. Shi, M. Li, Z. Zhang, Q. Yao, K. Shao, F. Xu, N. Xu, H. Li, J. Fan, W. Sun, J. Du, S. Long, J. Wang, X. Peng, Catalase-based liposomal for reversing immunosuppressive tumor microenvironment and enhanced cancer chemo-photodynamic therapy, Biomaterials 233 (2020), 119755.
[51] G. Li, S. Wang, D. Deng, Z. Xiao, Z. Dong, Z. Wang, Q. Lei, S. Gao, G. Huang, E. Zhang, G. Zeng, Z. Wen, S. Wu, Z. Liu, Fluorinated chitosan to enhance transmucosal delivery of sonosensitizer-conjugated catalase for sonodynamic bladder cancer treatment post-intravesical instillation, ACS Nano 14 (2) (2020) 1586–1599.
[52] S. Staehlke, H. Rebl, B. Finke, P. Mueller, M. Gruening, J.B. Nebe, Enhanced calcium ion mobilization in osteoblasts on amino group containing plasma polymer nanolayer, Cell Biosci. 8 (2018) 22.
[53] G. Meng, L. Pan, C. Li, F. Hu, X. Shi, I. Lee, I. Drevensek-Olenik, X. Zhang, J. Xu, Temperature-induced labelling of Fluo-3 AM selectively yields brighter nucleus in adherent cells, Biochem. Biophys. Res. Commun. 443 (3) (2014) 888–893.
[54] A. Perelman, C. Wachtel, M. Cohen, S. Haupt, H. Shapiro, A. Tzur, JC-1, Alternative excitation wavelengths facilitate mitochondrial membrane potential cytometry, Cell Death Dis. 3 (11) (2012), e430.
[55] L. Troiano, R. Ferraresi, E. Lugli, E. Nemes, E. Roat, M. Nasi, M. Pinti, A. Cossarizza, Multiparametric analysis of cells with different mitochondrial membrane potential during apoptosis by polychromatic flow cytometry, Nat. Protoc. 2 (11) (2007) 2719–2727.
[56] C.E. Callmann, L.E. Cole, C.D. Kusmierz, Z. Huang, D. Horiuchi, C.A. Mirkin, Tumor cell lysate-loaded immunostimulatory spherical nucleic acids as therapeutics for triple-negative breast cancer, Proc. Natl. Acad. Sci. U. S. A. 117 (30) (2020) 17543–17550.
[57] A.I. Petrov, D.V. Volodkin, G.B. Sukhorukov, Protein—calcium carbonate coprecipitation: a tool for protein encapsulation, Biotechnol. Prog. 21 (3) (2005) 918–925.
[58] P. Fadia, S. Tyagi, S. Bhagat, A. Nair, P. Panchal, H. Dave, S. Dang, S. Singh, Calcium carbonate nano- and microparticles: synthesis methods and biological applications, 3 Biotech 11 (11) (2021) 457.
[59] M.M. Longuinho, V. Ramnarain, N. Ortiz Peña, D. Ihiawakrim, R. Soria-Martínez, M. Farina, O. Ersen, A.L. Rossi, The influence of l-aspartic acid on calcium carbonate nucleation and growth revealed by in situ liquid phase TEM, CrystEngComm 24 (14) (2022) 2602–2614.
[60] A.R. Finney, R. Innocenti Malini, C.L. Freeman, J.H. Harding, Amino acid and oligopeptide effects on calcium carbonate solutions, Cryst. Growth Des. 20 (5) (2020) 3077–3092.
[61] H. Tong, W. Ma, L. Wang, P. Wan, J. Hu, L. Cao, Control over the crystal phase, shape, size and aggregation of calcium carbonate via a L-aspartic acid inducing process, Biomaterials 25 (17) (2004) 3923–3929.
[62] H. Adelnia, F. Sirous, I. Blakey, H.T. Ta, Metal ion chelation of poly(aspartic acid): from scale inhibition to therapeutic potentials, Int. J. Biol. Macromol. 229 (2023) 974–993.
[63] C. Qi, S. Musetti, L.H. Fu, Y.J. Zhu, L. Huang, Biomolecule-assisted green synthesis of nanostructured calcium phosphates and their biomedical applications, Chem. Soc. Rev. 48 (10) (2019) 2698–2737.
[64] V. Estrella, T. Chen, M. Lloyd, J. Wojtkowiak, H.H. Cornnell, A. Ibrahim-Hashim, K. Bailey, Y. Balagurunathan, J.M. Rothberg, B.F. Sloane, J. Johnson, R. A. Gatenby, R.J. Gillies, Acidity generated by the tumor microenvironment drives local invasion, Cancer Res. 73 (5) (2013) 1524–1535.
[65] X. Li, L. Yu, C. Zhang, X. Niu, M. Sun, Z. Yan, W. Wang, Z. Yuan, Tumor acid microenvironment-activated self-targeting & splitting gold nanoassembly for tumor chemo-radiotherapy, Bioact. Mater. 7 (2022) 377–388.
[66] T. Hotani, H. Mizuguchi, F. Sakurai, Systemically administered reovirus-induced downregulation of hypoxia inducible factor-1alpha in subcutaneous tumors, Mol. Ther. Oncolytics 12 (2019) 162–172.
[67] G. Santulli, W. Xie, S.R. Reiken, A.R. Marks, Mitochondrial calcium overload is a key determinant in heart failure, Proc. Natl. Acad. Sci. U. S. A. 112 (36) (2015) 11389–11394.
[68] P. Zheng, J. Ding, Calcium ion nanomodulators for mitochondria-targeted multimodal cancer therapy, Asian J. Pharm. Sci. 17 (1) (2022) 1–3.
[69] S. Bai, Y. Lan, S. Fu, H. Cheng, Z. Lu, G. Liu, Connecting calcium-based nanomaterials and cancer: from diagnosis to therapy, Nano-Micro Lett. 14 (1) (2022) 145.
[70] A. Ahmed, S.W.G. Tait, Targeting immunogenic cell death in cancer, Mol. Oncol. 14 (12) (2020) 2994–3006.
[71] L. Galluzzi, A. Buque, O. Kepp, L. Zitvogel, G. Kroemer, Immunogenic cell death in cancer and infectious disease, Nat. Rev. Immunol. 17 (2) (2017) 97–111.
[72] X. Xiong, J. Zhao, R. Su, C. Liu, X. Guo, S. Zhou, Double enhancement of immunogenic cell death and antigen presentation for cancer immunotherapy, Nano Today 39 (2021).
[73] H. Inoue, K. Tani, Multimodal immunogenic cancer cell death as a consequence of anticancer cytotoxic treatments, Cell Death Differ. 21 (1) (2014) 39–49.
[74] O. Krysko, T. Love Aaes, C. Bachert, P. Vandenabeele, D.V. Krysko, Many faces of DAMPs in cancer therapy, Cell Death Dis. 4 (5) (2013) e631.
[75] I. Ahmed, N. Ismail, M1 and M2 macrophages polarization via mTORC1 influences innate immunity and outcome of ehrlichia infection, J. Cell. Immunol. 2 (3) (2020) 108–115.
[76] J. Neefjes, M.L. Jongsma, P. Paul, O. Bakke, Towards a systems understanding of MHC class I and MHC class II antigen presentation, Nat. Rev. Immunol. 11 (12) (2011) 823–836.
[77] M. Wieczorek, E.T. Abualrous, J. Sticht, M. Alvaro-Benito, S. Stolzenberg, F. Noe, C. Freund, Major histocompatibility complex (MHC) class I and MHC class II proteins: conformational plasticity in antigen presentation, Front. Immunol. 8 (2017) 292.
[78] J.H. Lee, Injectable hydrogels delivering therapeutic agents for disease treatment and tissue engineering, Biomater. Res. 22 (2018) 27.
[79] T. Fang, X. Cao, B. Shen, Z. Chen, G. Chen, Injectable cold atmospheric plasma-activated immunotherapeutic hydrogel for enhanced cancer treatment, Biomaterials 300 (2023), 122189.
[80] J. Kim, D.M. Francis, L.F. Sestito, P.A. Archer, M.P. Manspeaker, M.J. O'Melia, S. N. Thomas, Thermosensitive hydrogel releasing nitric oxide donor and anti-CTLA-4 micelles for anti-tumor immunotherapy, Nat. Commun. 13 (1) (2022) 1479.
[81] D.Y. Kim, D.Y. Kwon, J.S. Kwon, J.H. Park, S.H. Park, H.J. Oh, J.H. Kim, B.H. Min, K. Park, M.S. Kim, Synergistic anti-tumor activity through combinational intratumoral injection of an in-situ injectable drug depot, Biomaterials 85 (2016) 232–245.
[82] R. Jaquilin P J, O.S. Oluwafemi, S. Thomas, A.O. Oyedeji, Recent advances in drug delivery nanocarriers incorporated in temperature-sensitive Pluronic F-127–A critical review, J. Drug Deliv. Sci. Technol. 72 (2022).
[83] M.R. Hight, E.T. Nolting Dd Fau - McKinley, A.D. McKinley Et Fau - Lander, S.K. Lander Ad Fau - Wyatt, M. Wyatt Sk Fau - Gonyea, P. Gonyea M Fau - Zhao, H.C.

Zhao P Fau - Manning, H.C. Manning, Multispectral Fluorescence Imaging to Assess pH in Biological Specimens, (1560-2281 (Electronic)) .
[84] P. Prasad, C.R. Gordijo, A.Z. Abbasi, A. Maeda, A. Ip, A.M. Rauth, R.S. DaCosta, X. Y. Wu, Multifunctional albumin–MnO2 nanoparticles modulate solid tumor microenvironment by attenuating hypoxia, acidosis, vascular endothelial growth factor and enhance radiation response, ACS Nano 8 (4) (2014) 3202–3212.
[85] T. Lin, Q. Zhang, A. Yuan, B. Wang, F. Zhang, Y. Ding, W. Cao, W. Chen, H. Guo, Synergy of tumor microenvironment remodeling and autophagy inhibition to sensitize radiation for bladder cancer treatment, Theranostics 10 (17) (2020) 7683–7696.
[86] P. Zhao, Y. Xu, W. Ji, S. Zhou, L. Li, L. Qiu, Z. Qian, X. Wang, H. Zhang, Biomimetic black phosphorus quantum dots-based photothermal therapy combined with anti-PD-L1 treatment inhibits recurrence and metastasis in triple-negative breast cancer, J. Nanobiotechnol. 19 (1) (2021) 181.
[87] I.X. Chen, K. Newcomer, K.E. Pauken, V.R. Juneja, K. Naxerova, M.W. Wu, M. Pinter, D.R. Sen, M. Singer, A.H. Sharpe, R.K. Jain, A bilateral tumor model identifies transcriptional programs associated with patient response to immune checkpoint blockade, Proc. Natl. Acad. Sci. U. S. A. 117 (38) (2020) 23684–23694.
[88] L. Solorio, H. Patel Rb Fau - Wu, T. Wu H Fau - Krupka, A.A. Krupka T Fau - Exner, A.A. Exner, Advances in Image-Guided Intratumoral Drug Delivery Techniques, (2041-5990 (Print)) .
[89] R.A. Sheth, R. Murthy, D.S. Hong, S. Patel, M.J. Overman, A. Diab, P. Hwu, A. Tam, Assessment of image-guided intratumoral delivery of immunotherapeutics in patients with cancer, JAMA Netw. Open 3 (7) (2020), e207911.
[90] A. Som, J.G. Rosenboom, A. Chandler, R.A. Sheth, E. Wehrenberg-Klee, Image-guided intratumoral immunotherapy: developing a clinically practical technology, Adv. Drug Deliv. Rev. 189 (2022), 114505.
[91] O. Chaudhuri, S.T. Koshy, C. Branco da Cunha, J.W. Shin, C.S. Verbeke, K. H. Allison, D.J. Mooney, Extracellular matrix stiffness and composition jointly regulate the induction of malignant phenotypes in mammary epithelium, Nat. Mater. 13 (10) (2014) 970–978.
[92] X. Han, Y. Li, Y. Xu, X. Zhao, Y. Zhang, X. Yang, Y. Wang, R. Zhao, G.J. Anderson, Y. Zhao, G. Nie, Reversal of pancreatic desmoplasia by re-educating stellate cells with a tumour microenvironment-activated nanosystem, Nat. Commun. 9 (1) (2018) 3390.
[93] J.H. Park, S.B. Jo, J.H. Lee, H.H. Lee, J.C. Knowles, H.W. Kim, Materials and extracellular matrix rigidity highlighted in tissue damages and diseases: implication for biomaterials design and therapeutic targets, Bioact. Mater. 20 (2023) 381–403.